Supplementary Material

1 RADIO TOMOGRAPHIC IMAGING ON PILOT

The PILOT mission concept uses a space-borne radio tomographic imaging system to produce rapidly refreshing (< 15 s) images of electron density with high spatial resolution ($\sim 0.5\ R_E$) over a large region of the inner magnetosphere (~ 3 hours of magnetic local time, ~ 3 L-shell in radial extent. These images allow detailed tracking and analysis of cold plasma mass flow, as well as the impact of these flows on magnetospheric subsystems.

Radio tomography combines well-established radio science techniques and computerized tomography (CT) to form rapidly refreshing images of electron density, essentially creating a motion picture of cold plasma. The core of radio tomographic imaging is to measure total electron content (TEC), using the measured phase shift between two radio signals, along a large set of lines-of-sight. As is done in CT medical imaging, the network of TEC measurements are then inverted to form an image.

Radio tomographic imaging on PILOT is summarized in Figure S1. Each of the RadioSat RT RF instruments transmits, one at a time, a coherently-phased pair of radio signals at two discrete frequencies that are received by all other RadioSat spacecraft. The measured phase difference, combined with the group delay between the two signals, yields an accurate measurement of TEC (Leitinger et al., 1997; Ergun et al., 2000). In < 15 s, each of the RadioSats has transmitted and received (Figure S1b), after which, the transmission cycle repeats. At any given time, four RadioSats are expected to be behind Earth (near perigee) relative to the bulk of the RadioSat constellation. Therefore 325 TEC measurements (and 325 redundant measurements) are expected, along with and 26 in-situ plasma density measurements from the 26 active RadioSat spacecraft. The 325 TEC measurements and 26 in-situ plasma density measurements produce an image of total electron density every $\sim$15 s (Figure S1c).

The plasma density distributions in Figure S1a and Figure S1b are extracted from IPE model simulation data (Maruyama et al., 2016). The image in Figure S1c is reconstructed solely from simulated TEC and in-situ density data (extracted from IPE model simulation data) using the inversion technique that is discussed below.

1.1 Measurement of TEC

Radio propagation experiments and extensive use of GPS signals have definitively demonstrated the ability to determine TEC using radio wave propagation (e.g., (Celnikier et al., 1983), (Morton et al., 2020) and references therein). The phase and group velocities of a radio signal propagating through a region of free electrons are well established (Ergun et al., 2000):

$$v_\phi = \frac{\omega}{k} \approx c\left(1 + \frac{\omega_{pe}^2}{2\omega^2}\right)\ ;\ v_g = \frac{d\,\omega}{d\,k} \approx c\left(1 - \frac{\omega_{pe}^2}{2\omega^2}\right) \tag{S1}$$

Here, ω is the radio signal angular frequency ($\omega = 2\pi f$), k is the wave vector, c is the speed of light and ω_{pe} is the plasma frequency. Also, $\omega_{pe}^2 = n_e e^2/\epsilon_0 m_e$, where n_e is the total electron plasma density, m_e is electron mass, e is the electron charge, and ϵ_0 is the permittivity of space). Radio signal phase advance (δt_ϕ) and group delay (δt_g) acquired during propagation over a distance L are linear with electron density:

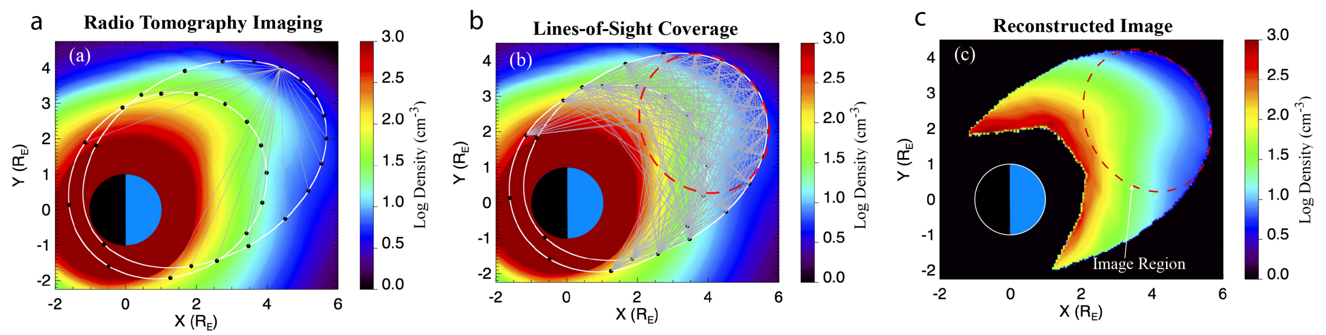

Figure S1. *A demonstration of radio tomographic imaging of plasma density. (a) A plasma density distribution in the inner magnetosphere extracted from IPE model simulation data (Maruyama et al., 2016). PILOT notional orbits are shown, with lines of sight from a single RadioSat spacecraft on the outer orbit to many other RadioSat spacecraft. (b) The full mesh of lines of sight between all PILOT RadioSats. The red circle indicates the region of nominal science $\sim 0.5 R_E$ resolution. (c) A plasma density image reconstructed using simulated line of sight TEC measurements through the modeled plasma density distribution.*

$$\delta t_\phi = -\frac{C}{\omega^2}\int_0^L n_e dl = -\frac{C}{\omega^2} TEC \; ; \; \delta t_g = \frac{C}{\omega^2}\int_0^L n_e dl = \frac{C}{\omega^2} TEC \; ; \; C = \frac{e^2}{2c\epsilon_0 m_e} \tag{S2}$$

Importantly, δt_ϕ and δt_g, are sensitive to the inverse of the radio wave frequency squared $(1/f^2)$. A dual-frequency carrier method avoids the necessity for highly accurate spacecraft position and radio transmission timing information. A low-frequency signal (f_L) is far more sensitive to TEC than a high frequency signal (f_H) so the TEC can be determined (Ergun et al., 2000) as:

$$TEC = \frac{4\pi^2}{C}\frac{f_H^2 f_L^2}{f_H^2 - f_L^2}\delta t_{\phi HL} \tag{S3}$$

Where $\delta t_{\phi HL}$ is the time delay between the two carrier frequencies. The two carrier frequencies can be precisely known and the time (phase) delay between them can be very accurately measured.

1.2 Radio Tomographic Image Reconstruction

Once TEC is measured between all spacecraft line of sight pairs and the data are received by ground stations, the plasma density image can be reconstructed. Image reconstruction for a space-borne system differs from that used in medical scans. Medical scans use circular line-of-sight meshes with high-resolution, well-defined angular coverage, and they deliberately oversample the image region. In space, one cannot arrange spacecraft in a perfect circle around a region of interest, and the number of unique lines-of-sight is limited to $(N^2 - N)/2$, where N is the number of satellites, so over-sampling requires an impractical number of spacecraft.

Electron density images are constructed from the TEC and in-situ density data using an iterative inversion technique. This technique produces an image with the least variance that satisfies the TEC and in-situ density measurements (Bernhardt et al., 1998; Ergun et al., 2000). As stated above, the two most important considerations are the spacing of the lines-of-sight and the angular coverage of the lines-of-sight. A two-orbit configuration provides the needed spacing and angular coverage for PILOT science.

The reconstruction algorithm for unevenly spaced lines-of-sight is iterative. An extended region between the spacecraft is gridded with $0.2\ R_E \times 0.2\ R_E$ pixels (the jagged region in Figure S1c). In inversion is not necessarily valid in the region outside the red dashed circle in Figure S1b, since there are many more pixels than lines of sight. To initialize, the pixels are assigned a previous image or a time-averaged value. Pixels that contain an in-situ measurement are fixed at the in-situ value of electron density.

To converge to a valid reproduction of the density, several image quality metrics are evaluated. TECError is the difference between the measured TEC and the TEC derived from the current iteration of the image for each line-of-sight. The lines of sight that are completely inside the red dashed circle in Figure S1b are given the highest weighting. The path length of each line-of-sight in each of the pixels is used in this evaluation. NeVar is the RMS normalized variation between all of the pixels and the surrounding four pixels. For each iteration, the pixels containing at least one line of sight are adjusted to partially reduce TECError and NeVar. The reduction is targeted at $\sim 50\%$ of the TECError. The image is then smoothed with higher weighting on pixels with the most lines-of-sight or an in-situ measurement. Each pixel is then assigned a random variation (percent), which, at first, dominates the changes. TECError and NeVar are then recalculated and the process is repeated. As the iteration advances, the random variations are slowly reduced. These random variations are needed to assure that reconstruction does not settle to a local minimum of TECError and NeVar.

The end result of the reconstruction is an image of the electron density that satisfies the TEC measurements with the least variance. This process avoids implanting aberrant features in an electron density image at the cost of possibly suppressing a real feature. By repeating the pseudo-random reconstruction multiple times, uniqueness can be tested and uncertainties can be quantified (Ergun et al., 2000).

2 INVERSION AND FORWARD MODEL ALGORITHMS FOR EUV IMAGE DECONVOLUTION

The PILOT EUVCS instrument provides global, line of sight integrated images of photons scattered by plasmaspheric He^+ at 30.4nm (EUV-He) and by O^+/O^{++} at 83.4nm (EUV-O). EUVCS images the meridional plane of the magnetosphere, orthogonal and complementary to the equatorial distribution obtained via radio tomography.

Inversion of EUV-He images extracts ion densities and convection flow velocities. From these flows, the corresponding convection E-field can be derived. Using IMAGE EUV data, several existing, well-established but less sophisticated techniques have demonstrated the basic capability to retrieve density and full 2D flow vectors (Goldstein et al., 2004; Goldstein and Sandel, 2005; Denton et al., 2006; Gallagher and Adrian, 2007). The full potential of EUV inversion was demonstrated by state-of-the-art, Bayesian/ Kalman inversion algorithms that yield the most robust inversions to date (Nakano et al., 2014b,a). Because global He^+ density is a reliable proxy for total plasma density (Goldstein et al., 2019, 2003), these improved methods to estimate density ($\pm 10\%$ inversion error) and electric field (± 0.2 mV/m) permit an accurate accounting of transport and loss of mass during erosion. The baseline method assumes the EUV-He imager is located outside the plasmapause, but previous work has demonstrated the ability to perform 'inside-out' inversion during times when the spacecraft is located within the main torus (Meier et al., 1998). Complementary PILOT in situ measurements provide validation of these EUV-He inversions, and firmly anchor the system-level estimates to microscale physics.

O^+ density structure differs from that of He^+ (Goldstein et al., 2019, 2018; Goldstein et al., 2022), so IMAGE EUV could not reveal global O^+ behavior. PILOT EUV-O fills this gap by measuring the global morphology and flows of O^+. In situ O^+ data provide cross checks of EUV-O images, and also reveal essential microphysics from density, temperature, and distribution function structure. PILOT's cross-scale O^+ observing will improve system-level constraints on models of O^+ dynamics. Existing forward modeling codes (e.g., Goldstein et al., 2018) are used to create simulated images, enabling iterative comparison with EUV-O images to constrain inversions. Reconstructing O^+ density from EUV images is challenging (Roelof et al., 1992); thus PILOT will need to mature its inversion/forward modeling algorithms during the mission (as IMAGE did) to account for complexities of interpreting 83.4-nm images such as earthshine, O^{++} ions, and temperature effects (Goldstein et al., 2018). Deconvolving O^+ / O^{++} is aided by PIMS's ability to distinguish O^{++}.

REFERENCES

Bernhardt, P. A., McCoy, R. P., Dymond, K. F., Picone, J. M., Meier, R. R., Kamalabadi, F., et al. (1998). Two-dimensional mapping of the plasma density in the upper atmosphere with computerized ionospheric tomography (CIT). *Physics of Plasmas* 5, 2010–2021. doi:10.1063/1.872872

Celnikier, L. M., Harvey, C. C., Jegou, R., Moricet, P., and Kemp, M. (1983). A determination of the electron density fluctuation spectrum in the solar wind, using the ISEE propagation experiment. *Astronomy and Astrophysics* 126, 293–298

Denton, R. E., Goldstein, J., Lee, D. H., King, R. A., Dent, Z. C., Gallagher, D. L., et al. (2006). Realistic magnetospheric density model for 29 August 2000. *Journal of Atmospheric and Solar-Terrestrial Physics* 68, 615–628. doi:10.1016/j.jastp.2005.11.009

Ergun, R. E., Larson, D. E., Phan, T., Taylor, D., Bale, S., Carlson, C. W., et al. (2000). Feasibility of a multisatellite investigation of the Earth's magnetosphere with radio tomography. *J. Geophys. Res.* 105, 361–374. doi:10.1029/1999JA900170

Gallagher, D. L. and Adrian, M. L. (2007). Two-dimensional drift velocities from the IMAGE EUV plasmaspheric imager. *Journal of Atmospheric and Solar-Terrestrial Physics* 69, 341–350. doi:10.1016/j.jastp.2006.05.028

Goldstein, J., Chappell, C. R., Davis, M. W., Denton, M. H., Denton, R. E., Gallagher, D. L., et al. (2018). Imaging the Global Distribution of Plasmaspheric Oxygen. *Journal of Geophysical Research (Space Physics)* 123, 2078–2103. doi:10.1002/2017JA024531

Goldstein, J., Gallagher, D., Craven, P. D., Comfort, R. H., Genestreti, K. J., Mouikis, C., et al. (2019). Temperature Dependence of Plasmaspheric Ion Composition. *Journal of Geophysical Research (Space Physics)* 124, 6585–6595. doi:10.1029/2019JA026822

Goldstein, J., Gallagher, D., Sandel, B., Davis, M., Molyneux, P., Veach, T., et al. (2022). Chapter 6 - the future of plasmaspheric extreme ultraviolet (euv) imaging. In *Understanding the Space Environment through Global Measurements*, eds. Y. Colado-Vega, D. Gallagher, H. Frey, and S. Wing (Elsevier). 231–286. doi:https://doi.org/10.1016/B978-0-12-820630-0.00010-6

Goldstein, J. and Sandel, B. R. (2005). The Global Pattern of Evolution of Plasmaspheric Drainage Plumes. *Washington DC American Geophysical Union Geophysical Monograph Series* 159, 1

Goldstein, J., Spasojević, M., Reiff, P. H., Sandel, B. R., Forrester, W. T., Gallagher, D. L., et al. (2003). Identifying the plasmapause in IMAGE EUV data using IMAGE RPI in situ steep density gradients. *Journal of Geophysical Research (Space Physics)* 108, 1147. doi:10.1029/2002JA009475

Goldstein, J., Wolf, R. A., Sandel, B. R., and Reiff, P. H. (2004). Electric fields deduced from plasmapause motion in IMAGE EUV images. *Geophysical Research Letters* 31, L01801. doi:10.1029/2003GL018797

Leitinger, R., Ladreiter, H. P., and Kirchengast, G. (1997). Ionosphere tomography with data from satellite reception of Global Navigation Satellite System signals and ground reception of Navy Navigation Satellite System signals. *Radio Science* 32, 1657–1669. doi:10.1029/97RS01027

Maruyama, N., Sun, Y.-Y., Richards, P. G., Middlecoff, J., Fang, T.-W., Fuller-Rowell, T. J., et al. (2016). A new source of the midlatitude ionospheric peak density structure revealed by a new Ionosphere-Plasmasphere model. *Geophysical Review Letters* 43, 2429–2435. doi:10.1002/2015GL067312

Meier, R. R., Nicholas, A. C., Picone, J. M., Melendez-Alvira, D. J., Ganguli, G. I., Reynolds, M. A., et al. (1998). Inversion of plasmaspheric EUV remote sensing data from the STP 72-1 satellite. *Journal of Geophysical Research* 103, 17505–17518. doi:10.1029/98JA01175

Morton, Y. J., Yang, Z., Breitsch, B., Bourne, H., and Rino, C. (2020). *Ionospheric Effects, Monitoring, and Mitigation Techniques* (John Wiley and Sons, Ltd), chap. 31. 879–937. doi:https://doi.org/10.1002/9781119458449.ch31

Nakano, S., Fok, M. C., Brandt, P. C., and Higuchi, T. (2014a). Estimation of temporal evolution of the helium plasmasphere based on a sequence of IMAGE/EUV images. *Journal of Geophysical Research (Space Physics)* 119, 3708–3723. doi:10.1002/2013JA019734

Nakano, S., Fok, M. C., Brandt, P. C., and Higuchi, T. (2014b). Estimation of the helium ion density distribution in the plasmasphere based on a single IMAGE/EUV image. *Journal of Geophysical Research (Space Physics)* 119, 3724–3740. doi:10.1002/2013JA019733

Roelof, E. C., Mauk, B. H., and Meier, R. R. (1992). Instrument requirements for imaging the magnetosphere in extreme ultraviolet and energetic neutral atoms derived from computer-simulated images. In *Instrumentation for Magnetospheric Imagery*, ed. S. Chakrabarti. vol. 1744 of *Society of Photo-Optical Instrumentation Engineers (SPIE) Conference Series*, 19–30. doi:10.1117/12.60576